5832 *Biochemistry* **2010,** *49,* 5832–5840
DOI: 10.1021/bi1000867

BIOCHEMISTRY
including biophysical chemistry & molecular biology
Article

^{1}H NMR Study of the Influence of Mutation on the Interaction of the C-Terminus with the Active Site in Heme Oxygenase from *Neisseria meningitidis*: Implications for Product Release[†]

Dungeng Peng,[‡] Li-Hua Ma,[‡] Hiroshi Ogura,[‡] En-Che Yang,[‡] Xuhong Zhang,[§] Tadashi Yoshida,[§] and Gerd N. La Mar*[,‡]

[‡]*Department of Chemistry, University of California, Davis, California 95616, and* [§]*Department of Biochemistry, Yamagata University School of Medicine, Yamagata 990-9585, Japan*

Received January 19, 2010; Revised Manuscript Received June 10, 2010

ABSTRACT: The HO from the pathogenic bacterium *Neisseria meningitidis*, *Nm*HO, possesses C-terminal His207, Arg208, and His209 residues that are undetected in crystal structures. NMR found the C-terminus ordered and interacting with the active site and shown to undergo a spontaneous cleavage of the C-terminal Arg208−His209 bond that affects the product off rate. A preliminary model for the interaction based on the wild-type (WT) *Nm*HO complexes has been presented [Liu, Y., Ma, L.-H., Satterlee, J. D., Zhang, X., Yoshida, T., and La Mar, G. N. (2006) *Biochemistry 45*, 3875−3886]. Two-dimensional ^{1}H NMR data of resting-state, azide-inhibited substrate complexes of the three C-terminal truncation mutants (Des-His209-, Des-Arg208His209-, and Des-His207Arg208His209-*Nm*HO) confirm the previous proposed roles for His207 and Arg208 and reveal important additional salt bridges involving the His209 carboxylate and the side chains of both Lys126 and Arg208. Deletion of His209 leads to a qualitatively retained C-terminal geometry, but with increased separation between the C-terminus and active site. Moreover, replacing vinyls with methyls on the substrate leads to a decrease in the separation between the C-terminus and the active site. The expanded model for the C-terminus reveals a less stable His207−Arg208 *cis* peptide bond, providing a rationalization for its spontaneous cleavage. The rate of this spontaneous cleavage is shown to correlate with the proximity of the C-terminus to the active site, suggesting that the closer interaction leads to increased strain on the already weak His207−Arg208 peptide bond. The relevance of the C-terminus structure for in vitro studies, and the physiological function of product release, is discussed.

The physiological catabolism of heme is conducted by the enzyme heme oxygenase (HO)[1] (*1*), which uses heme as both a substrate and a cofactor to stereoselectively cleave the porphyrin ring to yield biliverdin, iron, and CO. The enzyme is widely distributed, providing the key precursor to the antioxidant bilirubin, conserving iron and generating a neural messenger in mammals (*2*−*6*), producing a precursor to light-harvesting pigments in plants and photosynthetic bacteria (*7*), and serving as a scavenger for iron by some pathogenic bacteria (*2*, *4*). The various HOs exhibit the same mechanism that proceeds via the three intermediates *meso*-hydroxy heme, verdoheme, and iron-biliverdin (*2*−*6*), as shown in Figure 1. Three HO properties of particular interest are the strong stereoselectivity [only the α-meso position is cleaved in mammals (*1*)], the use of ferri-hydroperoxide (*8*, *9*), rather than the more common oxo-ferro group, to attack the *meso* position, and the exceedingly slow product (biliverdin) release (*10*) rate (0.03 s^{-1}). Crystal structures have revealed (*11*−*16*) a strongly conserved α-helical fold in spite of limited sequence homology. The stereoselectivity results from steric blocking of three *meso* positions and steric tilt/orientation of the exogenous ligand toward the fourth *meso* position. Destabilization of Fe^{3+}-OOH toward heterolytic O−O bond cleavage that yields the inactive oxo-ferryl group appears to result from the controlled, weak H-bonds to the exogenous ligand provided by a unique set of distal ordered water molecules imbedded within an extended H-bond network (*11*−*16*). The substrate is ligated by a His near the protein N-terminus such that the junction of two pyrroles is exposed to solvent, and with the C-terminus located in the proximity of the exposed heme edge, as illustrated in Figure 2A. The slow product off rate in mammalian HOs is strongly accelerated (*10*) upon formation of a 1:1 complex with biliverdin reductase (BVR), which is proposed (*17*) to dock HO near the exposed heme edge.

The HO from the pathogenic bacterium *Neisseria meningitidis* (*Nm*HO) (*2*, *18*) exhibits several distinct properties. The crystal structures of *Nm*HO substrate complexes reveal a typical α-helical fold as depicted in Figure 2A, in which the pyrrole A−D junction[2]

[†]This research was supported by National Institutes of Health Grant GM62830 (G.N.L.M.) and a grant-in-aid for Scientific Research from the Ministry of Education, Science, Culture, Sports, and Technology, Japan (16570108 to T.Y.).

*To whom correspondence should be addressed. E-mail: lamar@chem.ucdavis.edu. Phone: (530) 752-0958. Fax: (530) 752-8995.

[1]Abbreviations: DSS, 2,2-dimethyl-2-silapentane-5-sulfonate; EDTA, ethylenediaminetetraacetic acid; HO, heme oxygenase; *Nm*HO, *Neisseria meningitidis* heme oxygenase; ΔC1-*Nm*HO, Des-His209-*Nm*HO; ΔC2-*Nm*HO, Des-Arg208His209-*Nm*HO; ΔC3-*Nm*HO, Des-His207Arg208His209-*Nm*HO; PH, protohemin; DMDH, 2,4-dimethyldeuterohemin; BVR, biliverdin reductase; PDB, Protein Data Bank; NOE, nuclear Overhauser effect; NOESY, two-dimensional nuclear Overhauser spectroscopy; TOCSY, two-dimensional total correlation spectroscopy; ROESY, rotating frame two-dimensional nuclear Overhauser spectroscopy.

[2]Note that the conventions for labeling the four pyrroles A−D for protoporphyrin derivatives differ in crystallographic and other spectroscopic studies of hemoproteins. We utilize here the convention pyrrole-(substituent positions): A(1CH_3, 2-vinyl), B(3CH_3, 4-vinyl), C(5CH_3, 6-propionate), and D(7-propionate, 8CH_3).

 Published on Web 06/11/2010

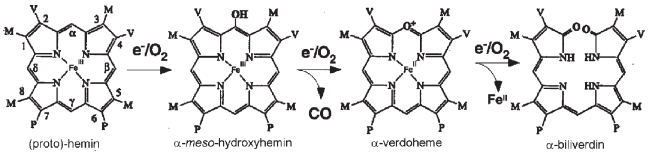

FIGURE 1: Intermediates in the catabolism of protohemin by heme oxygenase.

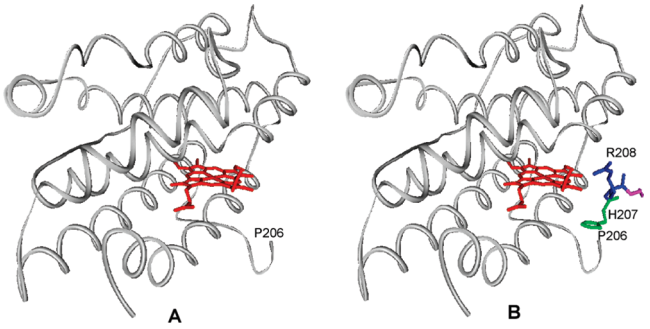

FIGURE 2: (A) Backbone of the crystal structure of *Nm*HO-PH-NO (PDB entry 1P3U) colored gray and PH substrate colored red. The crystallographically detected C-terminal residue is Pro206. (B) Imposed on the crystal structure are the solution ^{1}H NMR-characterized (*22*) His207 (green), whose peptide NH group is proposed to form an H-bond to the Asp27 carboxylate, and Arg208 (blue), whose guanidyl group makes a salt bridge with the 7-propionate carboxylate. The backbone of the C-terminal His209 is colored magenta; the positions of the free carboxylate and imidazole side chain were not addressed.

(see Figure 3) is exposed to solvent (*11*, *12*). Not detected in the crystal are the three C-terminal residues [His207, Arg208, and His209 (Figure 2A)], which were proposed to be structurally disordered. Solution ^{1}H NMR, a valuable adjunct to crystallography in confirming conserved (or modified) structure in solution, showed that the low-spin, cyanide- and azide-inhibited complexes of *Nm*HO (*19*−*21*) exhibited contacts with the exposed pyrrole A−D junction [i.e., $1CH_3$ and $8CH_3$ (see Figure 3)] for two residues not described in the crystal structures (*11*, *12*). The backbone $C_\beta H$ groups of a His exhibited NOEs to the $8CH_3$ and $1CH_3$ groups, and the $C_\alpha H$ group of another residue exhibited an intense NOE to the $8CH_3$ group. The assignment of the His detected in the crystal structure dictated (*19*) that the His in contact with the $1CH_3$ or $8CH_3$ group must arise from the crystallographically undetected C-terminal His207 or His209. Inspection of the crystal structures indicated stabilization of the C-terminal interaction could involve a salt bridge between the Arg208 guanidyl group and the substrate 7-propionate carboxylate, and a H-bond between the His207 peptide NH group and the carboxylate of Asp27, such that the $C_\beta H$ group of His207 and the $C_\alpha H$ group of Arg208 make contact with the exposed heme edge (*19*, *20*). On the basis of these NOESY contacts as constraints, limited energy minimization involving only His207 and Arg208 resulted in a model (*22*) of the C-terminal interaction of His207 and Arg208 with the active site as depicted in Figure 2B. It was not possible to obtain any NOESY constraints on His209, and hence, its role in the structure of the C-terminus remains obscure.

^{1}H NMR spectra, moreover, showed that all substrate complexes of *Nm*HO underwent a homogeneous "degradation" to a new species with altered hyperfine shifts (*20*−*22*), where the rate increased substantially upon replacement (*20*) of the vinyls in native protohemin [PH (R = vinyl in Figure 3)] with methyls in 2,4-dimethyldeuterohemin [DMDH (R = methyl in Figure 3)].

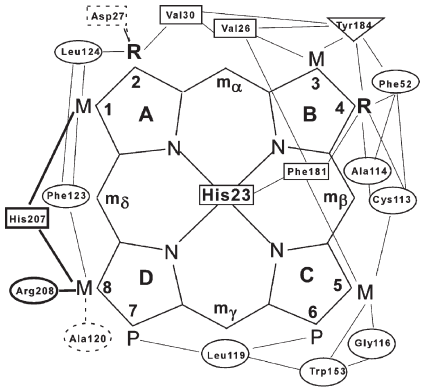

FIGURE 3: Structure of native protohemin [PH (R = vinyl)] oriented in the pocket of *Nm*HO as described in the crystal structures (*11*, *12*). The synthetic, 2-fold symmetric 2,4-dimethyldeuterohemin [DMDH (R = methyl)] is also shown; M = methyl, and P = propionate. Also shown are the crystallographically predicted substrate contact residues on the proximal (square), distal (circle), and equatorial (triangle) sides of the substrate. The two residues not observed in the crystal structure, but detected by ^{1}H NMR, His207 and Arg208, are shown in bold. Solid lines represent the crystallographically predicted, and ^{1}H NMR-observed, inter-residue and residue−substrate contacts; dashed lines represent the His207 and Arg208 contacts observed only in solution. The residues in dashed boxes are those predicted to be in contact with the pyrrole A−D junction (predicted contacts in dotted lines) but are too strongly relaxed to be detected in the azide complex.

The major distinction between the wild type (WT) and the degraded species was the loss of the contacts (*20*−*22*) between the exposed substrate edge and the proposed C-terminal His207Arg208 pair. Mass spectrometric and sequence data revealed (*22*) the degradation to be the spontaneous loss of Arg208 and His209. Preparation of recombinant Des-Arg208His209-*Nm*HO showed (*20*) it to be indistinguishable from the "degraded" *Nm*HO. The in vitro assay (*18*) using reduction with ascorbate and iron extraction with desferrioxamine revealed a doubling of the rate of biliverdin release upon cleavage of the C-terminus (*22*).

In view of the potential role of the C-terminus in modulating the rate of product release, we pursue here ^{1}H NMR studies of the substrate complexes of mutants of *Nm*HO designed to eliminate, in sequence, the three C-terminal residues that could interact with the active site. Our goals are to test our preliminary model (*22*) of the C-terminus interacting with the active site involving His207 and Arg208, as described in Figure 2B, characterize the potential role of the C-terminal His209 in this interaction, and gain some insight into the structural basis of the spontaneous C-terminal cleavage and the dependence of its rate on substrate vinyl versus methyl substituents (*20*). The ^{1}H NMR spectra of the physiologically relevant high-spin, resting-state, aquo complex resolve all substrate methyl signals, but extreme paramagnetic relaxation obscures all active site contact residues (*23*). Hence, it is highly advantageous to investigate the azide-inhibited complexes of the resting-state complex (*21*, *24*−*26*) which is unique in resolving the signals for the substrate methyls at the exposed edge of the substrate.

MATERIALS AND METHODS

Protein Preparation. The expression plasmids for the two new mutants, Des-His209-*Nm*HO (hereafter designated ΔC1-*Nm*HO) and Des-His207Arg208His209-*Nm*HO (hereafter designated ΔC3-*Nm*HO), were constructed by PCR methods similar to those reported previously (*22*) for the construction of Des-Arg208His209-*Nm*HO (hereafter designated ΔC2-*Nm*HO). Primers

for ΔC1-*Nm*HO and ΔC3-*Nm*HO contain a stop codon at the position of His209 and the position of His207, respectively. Wild-type *Nm*HO and the three mutants were prepared as described previously (*19*). Substrate complexes with both protohemin [PH (R = vinyl in Figure 3)] and 2,4-dimethyldeuterohemin [DMDH (R = methyl in Figure 3)] were prepared by titration to a 1:1 equivalent to substrate-free enzyme, followed by purification on a Sephadex 25 column eluted with 50 mM phosphate (pH ~7.2) and concentrated by ultrafiltration to give ~3 mM high-spin aquo complexes in 50 mM phosphate (pH 6.5). Azide in buffered solution was added to yield ~3 mM protein−substrate samples in 50 mM phosphate (pH ~7.2) with an ~25-fold excess of azide, except for the WT complex where samples were prepared in both 50 and 100 mM phosphate at pH 6.9−7.8.

NMR Spectroscopy. ^{1}H NMR data were collected on Bruker AVANCE 500 and 600 spectrometers operating at 500 and 600 MHz, respectively. Reference spectra were recorded in ^1H_2O over the temperature range of 25−35 °C at repetition rates of 1 s^{-1} over a spectral width of 50 ppm and at 5 s^{-1} over a spectral width of 200 ppm. Chemical shifts are referenced to 2,2-dimethyl-2-silapentane-5-sulfonate (DSS) through the water resonance calibrated at each temperature. The 600 MHz NOESY spectra (*27*) (mixing time of 40 ms, repetition rate of 1.5−2.5 s^{-1}) and 500 MHz Clean-TOCSY spectra (*28*) (to suppress ROESY response; 25°, 35 °C, spin lock of 25 ms, trim pulse of 2.5 s, repetition rate of 1−2 s^{-1}) were recorded over a bandwidth of 20 and 45 ppm (NOESY) and 20 ppm (TOCSY) using 512 t_1 blocks of 128 and 256 scans each consisting of 2048 t_2 points. Two-dimensional (2D) data sets were apodized by 30°- or 45°-sine-squared-bell functions and zero-filled to 2048 × 2048 data points prior to Fourier transformation.

Environmental Effects on C-Terminal Cleavage Rates. The rate of C-terminal cleavage of *Nm*HO−PH−H_2O split samples with 50 mM phosphate (pH 7.1) was followed by ^{1}H NMR, as described in detail previously (*22*), with one sample prepared with pretreatment of all glassware and columns with EDTA to remove adventitious trace metals. ^{1}H NMR was similarly used to follow C-terminal cleavage in the *Nm*HO−PH−H_2O split sample in 50 mM phosphate, one sample at pH 6.5 and the other at pH 7.5.

RESULTS

Spectral Comparisons. The low-field, resolved portions of the ^{1}H NMR spectra of high-spin, ferri-aquo PH complexes of WT *Nm*HO and the three deletion mutants are illustrated in Figure 4. The methyls and vinyl H_β atoms in the WT complex have been previously assigned (*23*) by steady-state NOEs and confirmed by cross-saturation between the azide and aquo complex (*21*). On the basis of spectral similarities shown in Figure 4, it appears reasonable to transfer the assignments from the WT to the deletion mutants. The assigned upfield vinyl $C_\beta H$ groups are not shown, but their chemical shifts, together with those of the assigned (*23*) methyl PH complexes, are listed in Table 1. Similar spectra for DMDH complexes are provided in Figure S1 of the Supporting Information. Chemical shifts for all substrate signals for high-spin complexes are also provided in Table S1 of the Supporting Information. Figure 5 displays the low-field portions of the ^{1}H NMR spectra of the WT *Nm*HO−DMDH azide complex and its three deletion mutants, which exhibit four resolved DMDH methyls, including the key $1CH_3$ and $8CH_3$ resonances; similar spectra for the PH complexes are provided in Figure S2 of the Supporting Information. The chemical shifts for DMDH and

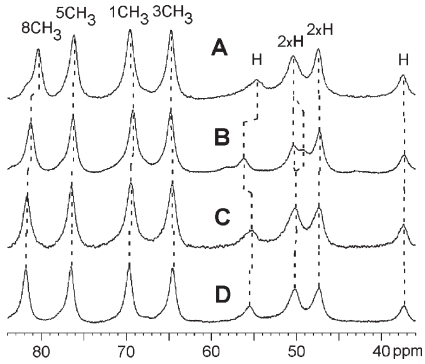

FIGURE 4: Low-field portion of the 500 MHz ^{1}H NMR spectra of high-spin (A) WT *Nm*HO−PH−H_2O, (B) ΔC1-*Nm*HO−PH−H_2O, (C) ΔC2-*Nm*HO−PH−H_2O, and (D) ΔC3-*Nm*HO−PH−H_2O complexes and 50 mM phosphate (pH ~7.2) at 25 °C, illustrating the positions of the four PH methyls (CH_3) and the six propionate/vinyl $C_\alpha H$ (H) signals. Methyl assignments have been reported (*23*) for the WT complex and can be transferred to the mutants on the basis of the high degree of spectral similarity.

Table 1: Substrate Chemical Shifts for the High-Spin *Nm*HO−PH−H_2O Complex and Its Three C-Terminal Truncation Mutants[a]

position	WT *Nm*HO[b]	ΔC1-*Nm*HO[c]	ΔC2-*Nm*HO[c]	ΔC3-*Nm*HO[c]
$8CH_3$	80.4	81.3	81.8	81.9
$5CH_3$	76.2	76.3	76.5	76.5
$1CH_3$	69.6	69.2	69.5	69.7
$3CH_3$	64.8	64.9	64.7	64.6
$2H_\beta$	−5.1	−5.3	−5.6	−5.6
$4H_\beta$	−8.5	−8.5	−8.6	−8.6
$2H_\beta$	−11.7	−11.3	−11.3	−11.5
$4H_\beta$	−15.0	−14.9	−14.9	−15.0

[a]Chemical shifts in parts per million, in H_2O and 50 mM phosphate (pH 7.0) at 25 °C, referenced to DSS via the residual solvent signal. [b]Chemical shifts and assignments taken from ref *23*. [c]The same assignments can be assumed for the three deletion mutants on the basis of the high degree of spectral similarity.

representative strongly upfield and downfield shifted residues for *Nm*HO−DMDH−N_3 complexes are given in Table 2, where we also include similar data (*21*) for the WT *Nm*HO−PH−N_3 complex; more complete assignments for the DMDH, as well as the analogous PH complexes, are provided in Tables S2 and S3 of the Supporting Information. Chemical shifts are given at 25 °C in 50 mM phosphate and found to be essentially invariant in the pH range of 6.9−7.8. For each ligand, Figures 4 and 5 and Tables 1 and 2 show that sizable substrate chemical shift perturbations are observed in the WT → ΔC1-*Nm*HO and ΔC1-*Nm*HO → ΔC2-*Nm*HO conversions, while only small, but still distinct, perturbations are observed in the ΔC2-*Nm*HO → ΔC3-*Nm*HO conversion; similar shift changes among the mutants are observed in the PH complexes (see Tables S2 and S3 of the Supporting Information).

Resonance Assignment. We emphasize assignments for the DMDH azide complexes that provide six identical (methyl) reporter groups on the active site environment and obviate any consideration of the effect of mutation on the perturbation of the substrate electronic structure by changes in vinyl group orientation. The individual DMDH methyl and propionate $C_\alpha H$ signals are identified by the expected pattern of NOESY cross-peaks (*20*, *26*, *29*) about the DMDH periphery, and the two symmetric portions of DMDH are readily differentiated by contacts to two

assigned residues that exhibit characteristic contacts between themselves [Val26/Tyr184 with $3CH_3/4CH_3$ (not shown); see Figure S3 of the Supporting Information], as described for the *Nm*HO−DMDH−CN complex (*20*). DMDH is 2-fold symmetric, but we chose to label positions 1−8 in Figure 3 on the basis of those positions occupied by PH in the crystal structure. Paramagnetic relaxation is sufficiently weak to allow appropriately tailored ^{1}H 2D NMR to provide (*21*) standard sequence-specific assignment (*30*) of helices of interest by N_i-N_{i+1}, α_i-N_{i+1}, β_i-N_{i+1}, α_i-N_{i+3}, and/or $\alpha_i-\beta_{i+3}$ NOESY contacts among TOCSY-detected spin systems (not shown; see Supporting Information, Figures S4 and S5) for residues with protons > 6 Å from the iron, as shown previously (*21*) for the *Nm*HO−PH−N_3 complex. Since the majority of assigned residues exhibit hyperfine shifts, the uniqueness of both TOCSY and NOESY connections is readily established using variable temperature as the "third dimension". These procedures provide the assignment of six helical fragments, Ala18−Val26, Cys113−Gly116, Phe123−Phe125, and Tyr137−Leu142 in ^1H_2O, and because of slow peptide exchange, fragments Phe52−Lys54 and Ala180, Phe181, Tyr184, and Val187 in ^2H_2O, in the same manner reported previously (*21*) for the *Nm*HO−DMDH−CN complex. This accounts for all of the residues [except Gly116 and Asp27 (vide infra)] predicted by the crystal structures to exhibit NOESY cross-peaks to DMDH (as depicted in Figure 3). In particular, NOESY data (not shown; see Figure S6 of the Supporting Information) show that pyrroles B and C exhibit only the contacts predicted by the crystal structures.

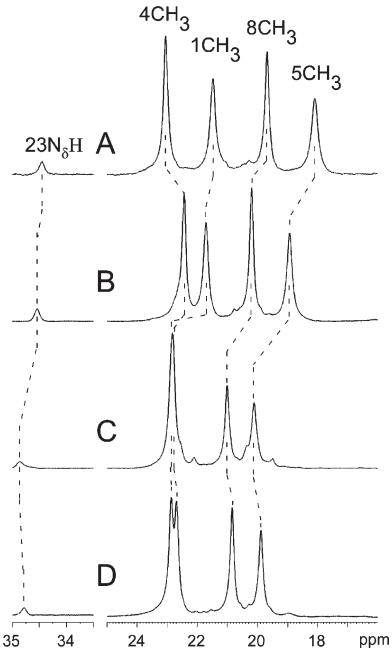

FIGURE 5: Low-field resolved portions of the ^{1}H NMR spectrum of (A) WT *Nm*HO−DMDH−N_3, (B) ΔC1-*Nm*HO−DMDH−N_3, (C) ΔC2-*Nm*HO−DMDH−N_3, and (D) ΔC3-*Nm*HO−DMDH−N_3 complexes in 50 mM phosphate (pH ~7.2) at 25 °C, illustrating the positions of the resolved DMDH methyls and axial His23 $N_\delta H$ resonances. Assignments determined here are based on the DMDH numbering in Figure 3.

Pyrrole A−D Contacts in the WT NmHO−DMDH−N_3 Complex. The pyrrole A−D junction is predicted (*11*, *12*) to exhibit relatively few contacts with active site residues as shown in Figure 3. NOESY spectra involving residues in contact with $1CH_3$ and $8CH_3$ for WT and the three deletion mutant DMDH azide complexes are illustrated in Figure 6. The intra- and interresidue contacts expected for the sequence-specifically assigned Phe123 and Leu124 in the WT *Nm*HO−DMDH−N_3 complex are illustrated in Figure 6A. The predicted contacts of Phe123 and Leu124 with $1CH_3$ and the contacts of Phe123 with $8CH_3$ are illustrated in panels B and B′ of Figure 6, respectively. Not observed are the predicted contacts between $8CH_3$ and Gly116 $C_\alpha H$ (4.5 Å from Fe) and $1CH_3$ and Asp27 $C_\alpha H$ and $C_\beta H$ (5.4 Å from Fe), for which strong paramagnetic relaxation (T_1 < 10 ms) precludes detection of NOESY cross-peaks. This accounts for the ^{1}H NMR detectable, and crystallographically predicted (*11*, *12*), contacts with the pyrrole A−D junction. Additionally, we detect a weakly relaxed His $C_\delta H$ in contact with its backbone (Figure 6A), and its $C_\beta H$ groups are in contact with both $1CH_3$ (Figure 6B)

Table 2: Chemical Shifts for Substrate and Key Residues in the WT *Nm*HO−DMDH−N_3 Complex and Its C-Terminal Truncation Mutants[a]

		DMDH				PH[b]
residue	position	WT *Nm*HO	ΔC1-*Nm*HO	ΔC2-*Nm*HO	ΔC3-*Nm*HO	WT *Nm*HO
DMDH	$1CH_3$	21.42	21.67	22.80	22.88	18.84
	$2CH_3$	10.10	10.85	12.32	12.22	10.22/0.29, −0.23[c]
	$3CH_3$	11.39	11.30	11.93	11.75	7.60
	$4CH_3$	23.00	22.42	22.74	22.67	11.78/−6.70, −7.01[c]
	$5CH_3$	18.05	18.95	20.06	19.89	18.02
	$8CH_3$	19.62	20.18	20.95	20.83	20.00
His23	$C_\alpha H$	6.12	6.25	5.95	6.02	6.28
	$C_\beta Hs$	9.28, 12.65	9.66, 13.04	9.57, 13.10	9.62, 13.09	9.68, 12.56
Val26	$C_\alpha H$	3.05	3.00	2.94	2.99	3.09
	$C_\beta H$	1.53	1.44	1.34	1.46	1.60
	$C_\gamma H_3s$	0.46, −1.13	0.39, −1.32	0.34, −1.30	0.38, −1.27	0.40, −1.13
Ala121	$C_\alpha H$	8.34	8.33	8.24	8.27	8.55
	$C_\beta H_3$	4.58	4.62	4.43	4.49	4.95
His207	$C_\alpha H$	3.65	3.90			3.74
	$C_\beta Hs$	1.38, 1.72	1.86, 2.11			1.56, 1.62
	$C_\delta H$	6.15	6.36			6.08
Arg208	$C_\alpha H$	3.85	3.70			3.83

[a]Chemical shifts, in parts per million, referenced to DSS via the solvent signal, in H_2O and 50 mM phosphate (pH 7.0) at 25 °C. [b]Data taken from ref *21*. [c]Vinyl positions in the order $C_\alpha H$, $C_\beta H$(*cis*), $C_\beta H$(*trans*).

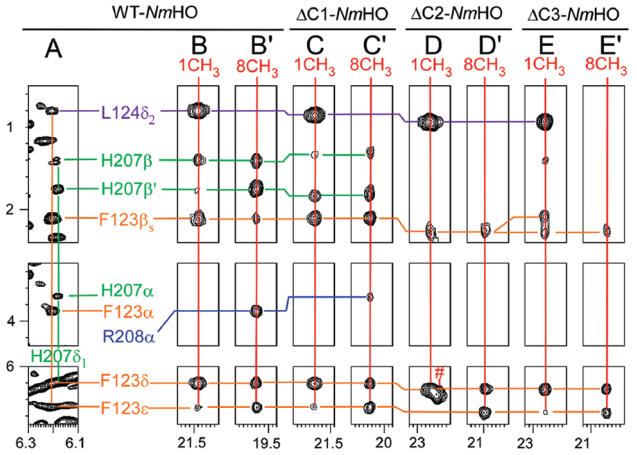

FIGURE 6: Portions of the 600 MHz ^{1}H NMR NOESY spectra illustrating the intra- and inter-residue contacts (mixing time of 40 ms, repetition rate of 1.0 s^{-1}) for Phe123 (orange), Leu124 (violet), and His207 (green) (A) and the contacts of these residues and Arg208 (blue) (mixing time of 40 ms, repetition rate of 2.5 s^{-1}) with $1CH_3$ (red) (B) and $8CH_3$ (red) (B′) of the WT *Nm*HO−DMDH−N_3 complex. The contacts between these residues and $1CH_3$ and $8CH_3$ are shown in panels C and C′ for the ΔC1-*Nm*HO−DMDH−N_3 complex, panels D and D′ for the ΔC2-*Nm*HO−DMDH−N_3 complex, and panels E and E′ for the ΔC3-*Nm*HO−DMDH−N_3 complex. The contacts with His207 and Arg208 are lost in both in the ΔC2- and ΔC3-*Nm*HO complexes. The complexes are in ^1H_2O and 50 mM phosphate (pH ∼7.2) at 25 °C. The number symbol designates the Phe52 C_ξH NOESY cross-peak to the $1CH_3$ signal, which is nearly degenerate with the $4CH_3$ signal (see Figure 5C and Figure S6 of the Supporting Information).

and $8CH_3$ (Figure 6B′). The C_αH of another weakly relaxed residue is in contact with $8CH_3$ (Figure 6B′). These two crystallographically undetected residues are the same as previously reported (*21*) for the PH complex and are attributed to His207 and Arg208, as described in the model in Figure 2B.

Hence, the qualitative model derived from ^{1}H NMR data for the PH complex (*22*) (Figure 2B) is also valid for the DMDH complex. However, we note that while the same pattern of NOESY cross-peaks from His207 and Arg208 to $8CH_3$ is observed in the DMDH and PH complexes, the intensity of the His207−$8CH_3$ NOESY cross-peaks, as illustrated in the slices of the NOESY spectra in panels A and B of Figure 7, is significantly increased upon replacement of vinyls with methyls. Thus, the C-terminus is closer to the substrate upon the replacement of substrate vinyls with methyls.

Pyrrole A−D Junction Contacts in the ΔC1-NmHO−DMDH−N_3 Complex. We observed the same inter- and intraresidue contacts for the crystallographically described Phe123 and Leu124, as well as C_δH to the backbone of a His (not shown; see Figure S7 of the Supporting Information), as observed in WT. The $1CH_3$ and $8CH_3$ NOESY contacts for this complex, shown in panels C and C′ of Figure 6, respectively, reveal not only the expected conserved contacts with Phe123 and Leu124 but also contacts with a His backbone (Figure 6C,C′); in addition, the C_αH of another residue forms a contact with $8CH_3$ (Figure 6C′). The deletion of His209 demands that the two C-terminal residues in contact with the active site in the ΔC1-*Nm*HO−DMDH−N_3 complex are indeed His207 and Arg208. The retention of the crystallographically undetected His207 and Arg208 contacts with the pyrrole A−D junction upon loss of His209 provides important but limited (vide infra) validation of the molecular model (*22*) in Figure 2B.

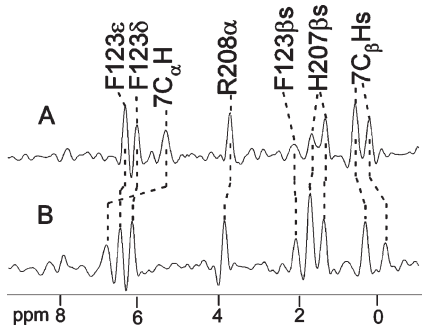

FIGURE 7: Slices through the $8CH_3$ peak in 600 MHz NOESY spectra (mixing time of 40 ms, repetition rate of 2 s^{-1}) for the WT (A) *Nm*HO−PH−N_3 and (B) *Nm*HO−DMDH−N_3 complexes in ^1H_2O and 50 mM in phosphate (pH 7.2) at 25 °C, illustrating the conserved cross-peak intensities to the 7-propionate C_αH and C_βHs, as well as Phe123, but the significant increase in intensity of the His207 C_βH−$8CH_3$ cross-peaks in the DMDH relative to the PH complex.

The pattern of His207 C_βH and Arg208 C_αH NOESY cross-peaks with the substrate is similar in ΔC1-*Nm*HO and WT *Nm*HO complexes of both DMDH (Figure 6B,B′,C,C′) and PH (not shown), but the intensity of the cross-peaks from the C-terminus to the $8CH_3$ is significantly weaker in the ΔC1-*Nm*HO−DMDH−N_3 complex (Figure 6C′) than in the WT *Nm*HO−DMDH−N_3 complex (Figure 6B′). Thus, the proximity of the C-terminus to the active site is significantly decreased after the loss of His209. Hence, the order of the proximity of the C-terminus to the substrate, as influenced by mutation or substrate substituents, is as follows: *Nm*HO−DMDH−N_3 > *Nm*HO−PH−N_3 > ΔC1-*Nm*HO−DMDH−N_3. We note that, in spite of exhibiting similar contacts between His207 and Arg208 and the pyrrole A−D junction in WT and ΔC1 *Nm*HO−DMDH−N_3 complexes (Figure 6C,C′,D,D′), the latter complex does not exhibit detectable C-terminal cleavage over a period of ∼100 h at 25 °C and dictates that the cleavage rate is retarded by a factor of > 10 in the ΔC1-*Nm*HO relative to WT *Nm*HO complex. Thus, the rate of C-terminal cleavage falls into the same pattern as the proximity of the C-terminus to the active site deduced above.

Pyrrole A−D Junction Contacts in the ΔC2- and ΔC3-NmHO−DMDH−N_3 Complexes. The $1CH_3$ and $8CH_3$ of both ΔC2-*Nm*HO−DMDH−N_3 (Figure 6D,D′) and ΔC3-*Nm*HO−DMDH−N_3 (Figure 6E,E′) complexes retain the Phe123 and Leu124 contacts, but both mutants lose the contacts with His207 and Arg208, as previously observed (*21*, *22*) for ΔC2-*Nm*HO−PH−N_3 and ΔC2-*Nm*HO−PH−CN complexes. This indicates that the majority of the interactions stabilizing the position of the C-terminus relative to the active site are lost upon deletion of Arg208. The data for the ΔC2-*Nm*HO complexes fail to provide any direct evidence of the existence of the proposed (*22*) His207 NH−Asp27 carboxylate H-bond. However, evidence of this interaction will be considered after the development of a more complete description of the interaction of the C-terminus in the active site of the WT complex (vide infra).

Environmental Effects on C-Terminal Cleavage. The rate of C-terminal cleavage of the *Nm*HO−DMDH−H_2O complex was found to be unaffected by pretreatment with EDTA, indicating that bond hydrolysis by adventitious metal ions is not responsible for the cleavage. The rate of cleavage did increase by a factor of ∼2 when the pH increased from 6.5 to 7.5, but this small effect can be attributed to the population (*31*) of the hydroxo complex at pH 7.5. Previously, we had reported (*22*) that the rate of cleavage was unaffected by

the exclusion of O_2 or the presence of mixtures of protease inhibitors.

DISCUSSION

The substrate hyperfine shifts exhibit significant changes upon the loss of His209 (compare WT and ΔC1-*Nm*HO complexes) and upon the subsequent loss of Arg208 (compare ΔC1-*Nm*HO and ΔC2-*Nm*HO complexes in Figures 4 and 5 and Tables 1 and 2); only small, but distinct, chemical shift changes are observed upon the subsequent loss of His207 (compare ΔC2-*Nm*HO and ΔC3-*Nm*HO complexes).

For high-spin aquo complexes, small perturbations on the substrate periphery tend to manifest themselves in small chemical shift changes for the substrate substituents in the immediate vicinity of the perturbations (vide infra). Azide complexes, on the other hand, possess an $S = {}^1/_2$ ground state and thermally populate the excited $S = {}^5/_2$ state (*32*, *33*) which can lead to "global" substrate chemical shift changes, dominated by the contact interaction (*21*, *33*−*35*), even though a perturbation may be well localized. Nonligated residues exhibit only dipolar shifts (*21*, *33*−*35*). Thus, conservation of chemical shifts for nonligated residues detected in the crystal structure dictates that the position of the residue and the anisotropy/orientation of χ be conserved upon mutation. Changes in the chemical shifts for the C-terminal residues upon mutation, when the orientation/anisotropy of χ is conserved (*36*), dictate a movement of the C-terminus relative to the active site.

Structure of the C-Terminus in WT NmHO and Effect of Deleting His209. The retention of the contacts between both $1CH_3$ and $8CH_3$ and the C_βHs of a terminal His, and the contact between $8CH_3$ and the C_αH of another C-terminal residue in ΔC1-*Nm*HO substrate azide complexes, unequivocally establishes that the exposed substrate edge contacts with the C-terminus in both WT and ΔC1-*Nm*HO involve His207 and Arg208. However, the separation between the C-terminus and active site is significantly increased in the ΔC1-*Nm*HO complex relative to the WT *Nm*HO complex, as evidenced by the reduced NOESY cross-peak intensities with the substrate (Figure 6). Moreover, while the dipolar shifts for the crystallographically described, nonligated residues are strongly conserved between WT *Nm*HO−DMDH−N_3 and ΔC1-*Nm*HO−DMDH−N_3 complexes (Table 2 and Table S2 of the Supporting Information) indicating that their geometry and orientation anisotropy of χ are conserved, the chemical shifts for His207 and Arg208 differ significantly for these two complexes (Table 2), indicating some movement of the C-terminus relative to the active site upon loss of His209. Therefore, His209 is not "innocent" but participates in some integral manner in stabilizing the interaction of the C-terminus with the active site.

An expanded depiction of the proposed model for the interaction of the C-terminus with the active site is shown in Figure 8; the substrate is colored red. Illustrated are the detected NOESY contacts (dashed line) between His207 C_βH (green) and $1CH_3$ and $8CH_3$ and the contact between Arg208 C_αH (blue) and $8CH_3$; the proposed salt bridge (arrow) between the Arg208 (blue) guanidyl group and the carboxylate of the 7-propionate (arrow) and the H-bond (arrow) between the His207 (green) peptide NH and the carboxylate of Asp27 (gray) are also shown. The initial model (*22*) defined only the position of the His209 backbone, with the C-terminal carboxylate and imidazole side chain orientations left undetermined. The His209 ring was detected (*22*) in the ^{1}H NMR spectrum of the WT *Nm*HO−PH−CN complex,

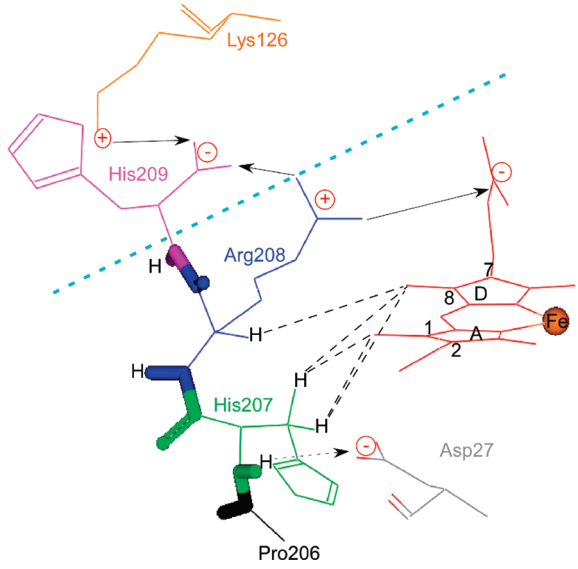

FIGURE 8: Enlarged and detailed view of the Pro206 (black) to Arg208 (blue) linkages for the molecular model of the C-terminus of substrate-bound *Nm*HO determined by limited energy minimization (*22*) (to the right and below the aqua dotted line) based on the proposed donor−acceptor interactions (arrows): His207 (green) peptide NH H-bond donor to carboxylate of Asp27 (gray) and the Arg208 (blue) guanidyl group salt bridges to the carboxylates of the 7-propionate (red). The distances of < 4 Å that account for the NOESY contacts to the $1CH_3$ and $8CH_3$ are shown by dashed lines. These 2D NMR data on deletion mutants confirm the previously proposed interactions and lead to the proposal of two additional salt bridges (arrow): C-terminal His209 (magenta) carboxylate and the side chain termini of both Arg208 (blue) and Lys126 (orange) (to the left and above the dotted line). The peptide bonds are depicted as tubes and show the positions of both the peptide NH and CO groups. Note that the His207−Arg208 peptide linkage is *cis*, rather than the more stable *trans*, and can be expected to favor selective cleavage at the His207−Arg208 bond.

but spectral congestion prevented the resolution of any NOESY cross-peaks to either its backbone or another residue.

Inspection of the crystal structures (*11*, *12*) and the preliminary model of the C-terminus (*22*), together with the presently observed weakening of the interaction of the C-terminus with substrate upon loss of His209, allows an expansion of the molecular model to encompass the structure of not only His209 but also Lys126. First, it is noted that the C-terminal His209 (magenta, in Figure 8) carboxylate in the preliminary model can occupy a rotational position that allows for a < 4 Å separation between one carboxylate O and one of the Arg208 (blue) guanidyl N_η atoms, and hence the formation of a robust salt bridge, as depicted by a solid arrow in Figure 8. Second, the terminus of Lys126 (orange), which the crystal structures (*11*, *12*) place on the surface with considerable allowable movement of its N-terminus, can, with only minor rearrangements of the side chain, place the terminal NH_3^+ group < 4 Å from the other O of the His209 (magenta) carboxylate and hence form an additional salt bridge, as shown by the solid arrow in Figure 8. Some support for the involvement of the Lys126 side chain terminus in the structure of the C-terminus can be drawn from some significant changes in the chemical shift of NOESY contacts with the His127 C_δH group (not shown) that are crystallographically predicted (*11*, *12*) to arise primarily from Lys126.

We propose that in WT *Nm*HO−substrate complexes the interaction of the C-terminus with the active site is stabilized by bifurcated salt bridges involving the Arg208 (blue) guanidyl group

with the carboxylates of both the 7-propionate (red) and Arg209 (magenta), and the His209 (magenta) carboxylate with both the Arg208 (blue) guanidyl group and the terminus of Lys126 (orange), as well as by the His207 (green) peptide NH H-bond to the carboxylate of Asp27 (gray), as depicted in Figure 8. Deletion of His209 from ΔC1-*Nm*HO complexes necessarily abolishes both salt bridges to its carboxylate. However, it is noted that, with some additional reorganization of the Lys126 terminus, a new salt bridge could be formed between the newly generated Arg208 carboxylate and the Lys126 side chain terminus in the ΔC1-*Nm*HO complex (not shown), such that the interaction of the C-terminus with the active site in WT and ΔC1-*Nm*HO complexes may differ by only a single salt bridge. The reduction of the number of pairwise stabilizing interactions can be expected to lead to weakening of the interaction between the C-terminus and the active site upon loss of His209, as observed. Lastly, the only significant chemical shift changes in the aquo complexes of PH upon loss of His209 are observed for $8CH_3$ (Figure 4 and Table 1) and 2-vinyl C_βHs (Table 1), consistent with the local effect of some movement of the C-terminal contacts to DMDH. In view of the apparent conservation of the geometry of the C-terminus upon deletion of His209, it is noteworthy that the rate of subsequent cleavage of the His207−Arg208 peptide bond is retarded relative to those of WT *Nm*HO substrate complexes by a factor of >10.

Effect of Deleting Arg208 on the Active Site. The most dramatic structural changes in the interaction of the C-terminus with the active site occur upon the subsequent loss of Arg208. Thus, not only is the Arg208 C_αH cross-peak to $8CH_3$ necessarily missing, but the His207 C_βH cross-peaks to both $1CH_3$ and $8CH_3$ are also lost, indicating a very substantial disruption of the C-terminal interaction with the active site. Assuming that the salt bridge from the Lys126 terminus to the Arg208 carboxylate exists in ΔC1-*Nm*HO complexes, the loss of Arg208 eliminates two of the three remaining interactions, leaving only the potential His207 peptide NH H-bond to the Asp27 carboxylate, which must be insufficiently strong to clearly retain the interaction of His207 with the substrate. Evidence of the His207 NH−Asp27 carboxylate H-bond in the WT complex will be considered later (vide infra). The *Nm*HO−PH−H_2O complexes again reveal the largest chemical shift changes for $8CH_3$ and 2-vinyl H_βs (Table 1), consistent with the local loss of contacts.

Effect of Deleting His207 on the Active Site. The data described above provide direct support for the interaction of the Arg208 side chain with the active site. However, the only NOESY cross-peaks to substrate in ΔC2-*Nm*HO complexes are those predicted by the crystal structures; we were unable to locate the His207 signals. Inspection of all NMR data (Tables 1 and 2) indicates that the loss of His207 results in the smallest, albeit distinct, chemical shift changes for the substrate. These chemical shift perturbations indicate that the active site "senses" His207 and are unlikely to result if His207 were oriented wholly toward the solvent in ΔC2-*Nm*HO−substrate complexes. A scenario that could account for the observation involves an equilibrium between a weakly populated state in which His207 is oriented into, and interacts with, the active site and a more extensively populated state in which His207 is oriented out toward the solvent. Dynamics of the interconversion on the NMR time scale (*37*) would broaden the His ring signals and preclude detection of either the His207 ring signals directly or any weak NOESY cross-peaks to the $1CH_3/8CH_3$ but still result in the perturbation of the DMDH chemical shifts upon deletion of His207. The only chemical shift perturbations (Table 1) outside of the uncertainties (±0.05 ppm) in the high-spin, aquo complex are for the 2-vinyl H_β in contact with Asp27.

Evidence of the His207 NH H-Bond. The initially proposed peptide NH H-bond from His207 to the Asp27 carboxylate was based on strong low-field bias for the His207 peptide chemical shift in the cyanide complex (*20*); more rapid exchange with solvent precludes detection of the His207 NH in the azide complexes. It was noted (*20*, *22*), however, that the optimal orientation of the Asp27 carboxylate for this H-bond was sterically blocked by the out-of-plane orientation of the 2-vinyl group. The smaller separation between the C-terminus and substrate upon replacement of PH with DMDH, as evidenced in the stronger His207−$8CH_3$ NOESY cross-peaks in Figure 7, is attributed to the optimization, upon replacement of vinyls with methyls, of the Asp27 carboxylate orientation as an acceptor for the His207 peptide NH. This change in structure is supported by significant chemical shift changes for His207 (Table 2), while the anisotropy/orientation of χ (chemical shift for nonligated residues) is conserved.

The conversion of the WT *Nm*HO−PH−H_2O complex to the ΔC1-*Nm*HO−PH−H_2O complex results in selective chemical shift changes for $1CH_3$, $8CH_3$, and 2-vinyl C_βHs (Figure 4 and Table 1), indicating that a perturbation occurs not only for the pyrrole A−D junction but also at the 2-vinyl in contact with the Asp27 side chain. Similarly, the loss of His207 results in selective chemical shift changes for the 2-vinyl H_β and $1CH_3$ in contact with His207.

Structure of the C-Terminus Relevant to Cleavage. The mechanism of cleavage is incompletely understood; the rate is fastest in the aquo complex (*20*, *22*), is strongly retarded by strong field ligands, and is significantly modulated by porphyrin substituents [DMDH complexes cleave much faster than PH complexes (*20*)]. Only a very weak pH effect is observed, and the rate is unaffected by the presence of EDTA (to sequester adventitious metal ions), protease inhibitors, or molecular oxygen (*22*).

The degradation of WT substrate complexes of *Nm*HO produced only ΔC2-*Nm*HO, with no detectable ΔC1-*Nm*HO (*20*, *22*). This observation is equally consistent with two one-residue cleavages, with the second rate (for Arg208) much faster than the first (for His209), or a single cleavage of the Arg208His209 dipeptide. The presently observed strong retardation of further cleavage of ΔC1-*Nm*HO forms to yield ΔC2-*Nm*HO establishes that the His207−Arg208 peptide bond is cleaved in one step. Inspection of the molecular model for the C-terminal interaction with the active site in Figure 8 reveals the uncommon *cis* peptide linkage for the His207−Arg208 bond. The *trans* linkage precluded the interaction of the terminus of Arg208 with the substrate (*20*). The *cis* peptide bond is intrinsically less stable (*38*) than the *trans* bond, providing a rationalization for the cleavage of an intact dipeptide.

The modulation of the rate of C-terminal cleavage (observed as *Nm*HO−DMDH−H_2O > *Nm*HO−PH−H_2O > ΔC1-*Nm*HO−PH−H_2O) correlates directly with the deduced degree of separation between the C-terminus and the active site, as reflected in the intensity of the His207−$8CH_3$ NOESY cross-peaks, suggesting that the movement of His207 closer to the $8CH_3$ puts additional strain on the His207−Arg208 *cis* peptide bond. The fastest cleavage rate for the physiologically relevant resting-state complex (*Nm*HO−PH−H_2O) has a half-life of ~24 h (*22*), which is much too long to have any true functional relevance, since substrate binding is rapidly followed by catabolism of the heme

in vivo. Therefore, the spontaneous cleavage of the His207−Arg208 peptide bond must be considered an artifact of the in vitro handling of the protein.

Functional Implications for the C-Terminal Structure. The ^{1}H NMR-characterized interaction of the C-terminus with the active site in *Nm*HO substrate complexes has significance for both the in vitro characterization of the enzyme on the basis of which the functional properties are interpreted and the in vivo process of product release. On one hand, the spontaneous cleavage of the His207−Arg208 peptide bond with a half-life of <24 h can result in detailed physicochemical characterization of a "damaged" enzyme. We have already shown that the ligand affinity is halved and product biliverdin release rate is doubled (*22*) upon loss of the C-terminus. The failure to detect the three C-terminal residues in the crystal structures (*11*, *12*) of *Nm*HO−PH complexes may be due to a disordered structure of the C-terminus in crystals, but it could as well have resulted from the cleavage of the C-terminus during the processing and subsequent crystallization of *Nm*HO. The half-life for cleavage (∼24 h) is short compared to the time to generate crystals (∼7 days). While the pH and buffer concentration are similar for the solution NMR and crystal studies, the effect of polyethylene glycol used in the latter studies on the rate of cleavage is not known. It is necessary to monitor the polypeptide by mass spectrometry during any in vitro characterization of *Nm*HO.

On the other hand, the structure of the C-terminus can be expected to have implications for the function of *Nm*HO. The release of product by HOs is very slow and is strongly accelerated upon formation of 1:1 complexes with BVR in mammalian HOs (*10*). The product HemO iron(III)-biliverdin complex inhibits heme oxygenase activity (*18*). The need to protect *N. meningitidis* from the toxic effects of hemin, together with the unacceptably slow rate of turnover for purified HemO (*2*, *18*), indicates the existence of some, as yet unidentified, effector protein analogue to the mammalian BVR that facilitates release of iron and/or biliverdin. The docking of a BVR analogue with *Nm*HO is also likely to occur at the exposed edge of *Nm*HO substrate complexes, precisely the location of the C-terminal residues. The demonstrated interaction of the C-terminus with the active site (*19*, *20*, *22*), together with the observed change in axial ligand affinity and product loss rate (*22*), allows for the reasonable supposition of the involvement of the C-terminus in modulating product release in HemO. The exact nature of the role in product release will become clear only upon identification of the analogue to BVR in pathogenic bacteria. A more detailed structure determination of the intact WT *Nm*HO−substrate complex will be necessary, via crystallography or three-dimensional (3D) NMR on a ^{15}N- and ^{13}C-labeled *Nm*HO. To date, a prepared [^{15}N]*Nm*HO exhibited extensive cleavage over the duration of the required 3D experiment. A better understanding of the cleavage mechanism will likely provide the necessarily stable complexes. Alternatively, the ΔC1-*Nm*HO substrate complex, which is considerably more resistant to C-terminal cleavage, could serve as an ideal subject for either crystallography or, upon ^{15}N and ^{13}C labeling, 2D and 3D NMR studies.

CONCLUSIONS

Solution ^{1}H NMR spectra of paramagnetic *Nm*HO substrate complexes provide unique insight into the interaction of the C-terminus with the active site, where structural changes upon sequential C-terminal deletions can be monitored both by changes in spatial contacts between the residues and the active site and by changes in the hyperfine shift patterns of the substrate. 2D NMR data for WT and C-terminal deletion mutants of *Nm*HO, together with molecular modeling, indicate that the interactions of the C-terminus with the active site consist of three salt bridges and one H-bond. The cationic carboxylate of His209 forms salt bridges to the termini of both Lys126 and Arg208, with the Arg208 terminus forming an additional salt bridge to the carboxylate of the 7-propionate; the peptide NH group of His207 forms an H-bond with the carboxylate of Asp27.

Deletion of the C-terminal His209 necessarily abolishes both salt bridges to the His209 carboxylate, but the newly generated Arg208 carboxylate is in a position to form a salt bridge with the terminus of Lys126. The geometry of the C-terminus relative to the active site is largely conserved upon deletion of His209, but the loss of a key salt bridge yields a significantly "looser" interaction between the C-terminus and the active site. Subsequent deletion of Arg208 necessarily abolishes the two remaining salt bridges but leaves the His207−Asp27 H-bond as a potential stabilizing interaction. The failure to detect interaction between His207 and the active site is consistent with either a relatively weak H-bond relative to the salt bridges or an H-bond that forms only cooperatively with the two Arg208 salt bridges. The presence of this H-bond in WT *Nm*HO is supported by a strong influence of substrate substituents on the C-terminal to substrate spacing.

The structure of the C-terminus shows that the His207−Arg208 peptide bond is in the less stable *cis* rather than the more stable and more conventional *trans* configuration. This likely accounts for the spontaneous, selective loss of the Arg208−His209 dipeptide bond for substrate complexes of *Nm*HO. The significant retardation of the rate of C-terminal cleavage upon loss of His209 and the enhancement in this rate upon replacement of substrate vinyls with methyls correlate with the deduced "tightness" of the interaction of the C-terminus with the active site, which may place additional strain on the His207−Arg208 *cis* peptide bond. The very slow cleavage rates make the phenomenon physiologically irrelevant but can seriously limit the significance of in vitro physicochemical studies if the integrity of the His207−Arg209 bond is not verified by mass spectrometry. The novel interaction of the C-terminus with the active site is implicated in the mechanism for the controlled transfer of the toxic biliverdin product to the analogue of the mammalian biliverdin reductase that docks with HO at the exposed substrate edge.

SUPPORTING INFORMATION AVAILABLE

Three tables (chemical shifts for *Nm*HO−DMDH-H_2O, *Nm*HO−DMDH-N_3 and *Nm*HO-PH-N_3 complexes), and seven figures (^{1}H NMR spectra for *Nm*HO−DMDH-H_2O and *Nm*HO-PH-N_3 complexes, TOCSY spectrum for *Nm*HO−DMDH, NOESY assignment of DMDH, NOESY spectra for the proximal helix, NOESY contacts to pyrroles B/C junction and substrate methyl contacts for ΔC1-*Nm*HO−DMDH-N_3). This material is available free of charge via the Internet at http://pubs.acs.org.

REFERENCES

1. Tenhunen, R., Marver, H. S., and Schmid, R. (1969) Microsomal heme oxygenase. Characterization of the enzyme. *J. Biol. Chem. 244*, 6388–6394.
2. Wilks, A. (2002) Heme Oxygenase: Evolution, Structure, and Mechanism. *Antioxid. Redox Signaling 4*, 603–614.
3. Ortiz de Montellano, P. R., and Auclair, K. (2003) Heme Oxygenase Structure and Mechanism. In The Porphryin Handbook (Kadish, K. M., Smith, K. M., and Guilard, R., Eds.) pp 175−202, Elsevier Science, San Diego.

4. Frankenberg-Dinkel, N. (2004) Bacterial Heme Oxygenases. *Antioxid. Redox Signaling 6*, 825–834.
5. Rivera, M., and Zeng, Y. (2005) Heme oxygenase, steering dioxygen activation toward heme hydroxylation. *J. Inorg. Biochem. 99*, 337–354.
6. Unno, M., Matsui, T., and Ikeda-Saito, M. (2007) Structure and catalytic mechanism of heme oxygenase. *Nat. Prod. Rep. 24*, 553–570.
7. Beale, S. I. (1994) Biosynthesis of open-chain tetrapyrroles in plants, algae, and cyanobacteria. *Ciba Found. Symp. 180*, 156–168.
8. Wilks, A., Torpey, J., and Ortiz de Montellano, P. R. (1994) Evidence for the electrophilic oxygen addition to the porphyrin ring in the formation of α-meso-hydroxyheme. *J. Biol. Chem. 269*, 29553–29556.
9. Davydov, R. M., Yoshida, T., Ikeda-Saito, M., and Hoffman, B. M. (1999) Hydroperoxy-Heme Oxygenase Generated by Cryoreduction Catalyzes the Formation of α-*meso*-Hydroxyheme as Detected by EPR and ENDOR. *J. Am. Chem. Soc. 121*, 10656–10657.
10. Liu, Y., and Ortiz de Montellano, P. R. (2000) Reaction Intermediates and Single Turnover Rate Constants for the Oxidation of Heme by Human Heme Oxygenase-1. *J. Biol. Chem. 275*, 5297–5307.
11. Schuller, D. J., Zhu, W., Stojiljkovic, I., Wilks, A., and Poulos, T. L. (2001) Crystal structure of heme oxygenase from the Gram-negative pathogen *Neisseria meningitidis* and a comparison with mammalian heme oxygeanse-1. *Biochemistry 40*, 11552–11558.
12. Friedman, J. M., Lad, L., Deshmukh, R., Li, H. Y., Wilks, A., and Poulos, T. L. (2003) Crystal structures of the NO- and CO-bound heme oxygenase from *Neisseriae meningitidis*: Implications for O_2 activation. *J. Biol. Chem. 278*, 34654–34659.
13. Lad, L., Wang, J., Li, H., Friedman, J., Bhaskar, B., Ortiz de Montellano, P. R., and Poulos, T. L. (2003) Crystal Structures of the Ferric, Ferrous and Ferrous-NO Forms of the Asp140Ala Mutant of Human Heme Oxygenase-1: Catalytic Implications. *J. Mol. Biol. 330*, 527–538.
14. Sugishima, M., Sakamoto, H., Noguchi, M., and Fukuyama, K. (2003) Crystal Structures of CO-, CN-, and NO-Bound Forms of Rat Heme Oxygenase-1 (HO-1) in Complex with Heme: Structural Implications for Discrimination between CO and O_2 in HO-1. *Biochemistry 42*, 9898–9905.
15. Unno, M., Matsui, T., Chu, G. C., Coutoure, M., Yoshida, T., Rousseau, D. L., Olson, J. S., and Ikeda-Saito, M. (2004) Crystal Structure of the Dioxygen-bound Heme Oxygenase from *Corynebacterium diphtheriae*. *J. Biol. Chem. 279*, 21055–21061.
16. Friedman, J., Lad, L., Li, H., Wilks, A., and Poulos, T. L. (2004) Structural Basis for Novel δ-Regioselective Heme Oxygenation in the Opportunistic Pathogen *Pseudomonas aeruginosa*. *Biochemistry 43*, 5239–5245.
17. Wang, J., and Ortiz de Montellano, P. R. (2003) The Binding Sites on Human Heme Oxygenase-1 for Cytochrome P450 Reductase and Biliverdin Reductase. *J. Biol. Chem. 278*, 20069–20076.
18. Zhu, W., Willks, A., and Stojiljkovic, I. (2000) Degradation of heme in Gram-negative bacteria: The product of the hemO gene of *Neisseriae* is a heme oxygenase. *J. Bacteriol. 182*, 6783–6790.
19. Liu, Y., Zhang, X., Yoshida, T., and La Mar, G. N. (2004) ^{1}H NMR characterization of the solution active site structure of substrate-bound, cyanide-inhibited heme oxygenase from *Neisseria meningitidis*: Comparison to crystal structures. *Biochemistry 43*, 10112–10126.
20. Liu, Y., Ma, L.-H., Zhang, X., Yoshida, T., Satterlee, J. D., and La Mar, G. N. (2006) ^{1}H NMR study of the influence of hemin vinyl-methyl substitution on the interaction between the C-terminus and substrate and the "aging" of the heme oxygenase from *N. meningitidis*. Induction of active site structural heterogeneity by a two-fold symmetric hemin. *Biochemistry 45*, 13875–13888.
21. Ma, L.-H., Liu, Y., Zhang, X., Yoshida, T., and La Mar, G. N. (2009) ^{1}H NMR study of the effect of variable ligand on heme oxygenase electronic and molecular structure. *J. Inorg. Biochem. 103*, 10–19.
22. Liu, Y., Ma, L.-H., Satterlee, J. D., Zhang, X., Yoshida, T., and La Mar, G. N. (2006) Characterization of the spontaneous "aging" of the heme oxygenase from the pathological bacterium *Neisseria meningitidis* via cleavage of the C-terminus in contact with the substrate: Implications for functional studies and the crystal structure. *Biochemistry 45*, 3875–3886.
23. Liu, Y., Zhang, X., Yoshida, T., and La Mar, G. N. (2005) Solution ^{1}H NMR characterization of the distal H-bond network and the effective axial field in the resting-state, high-spin ferric, substrate-bound complex of heme oxygenase from *N. meningitidis*. *J. Am. Chem. Soc. 127*, 6409–6422.
24. Zeng, Y., Caignan, G. A., Bunce, R. A., Rodriguez, J. C., Wilks, A., and Rivera, M. (2005) Azide-inhibited Bacterial Heme Oxygenases Exhibit an $S = 3/1$ $(d_{xz},d_{yz})^3(d_{xy})^1(d_{z^2})^1$ Spin State: Mechanistic Implications for Heme Oxidation. *J. Am. Chem. Soc. 127*, 9794–9807.
25. Rodriguez, J. C., Wilks, A., and Rivera, M. (2006) Backbone NMR Assignments and H/D Exchange Studies on the Ferric Azide- and Cyanide-Inhibaited Forms of *Pseudomonas aeruginosa* Heme Oxygenase. *Biochemistry 45*, 4578–4592.
26. Ogura, H., Evans, J. P., Peng, D., Satterlee, J. D., Ortiz de Montellano, P. R., and La Mar, G. N. (2009) The Orbital Ground State of the Azide-Substrate Complex of Human Heme Oxygenase Is an Indicator of Distal H-Bonding: Implications for the Enzyme Mechanism. *Biochemistry 48*, 3127–3132.
27. Jeener, J., Meier, B. H., Bachmann, P., and Ernst, R. R. (1979) Investigation of Exchange Processes by Two Dimensional NMR Spectroscopy. *J. Chem. Phys. 71*, 4546–4553.
28. Griesinger, C., Otting, G., Wüthrich, K., and Ernst, R. R. (1988) Clean TOCSY for ^{1}H Spin System Identification in Macromolecules. *J. Am. Chem. Soc. 110*, 7870–7872.
29. Li, Y., Syvitski, R. T., Chu, G. C., Ikeda-Saito, M., and La Mar, G. N. (2003) Solution ^{1}H NMR investigation of the active site molecular and electronic structures of the substrate-bound, cyanide-inhibited bacterial heme oxygenase from *C. diphtheriae*. *J. Biol. Chem. 279*, 6651–6663.
30. Wüthrich, K. (1986) NMR of Proteins and Nucleic Acids, Wiley & Sons, New York.
31. Ma, L.-H., Liu, Y., Zhang, X., Yoshida, T., and La Mar, G. N. (2006) ^{1}H NMR Study of the Magnetic Properties and Electronic Structure of the Hydroxide Complex of Substrate-Bound Heme Oxygenase from *N. meningitidis*: Influence of the Axial Water Deprotonation on the Distal H-bond Network. *J. Am. Chem. Soc. 128*, 6657–6668.
32. Morishima, I., Ogawa, S., Inubushi, T., and Iizuka, T. (1978) Nuclear Magnetic Resonance Studies of High-Spin Ferric Hemoproteins. *Adv. Biophys. 11*, 217–245.
33. La Mar, G. N., Satterlee, J. D., and de Ropp, J. S. (2000) NMR of Hemoproteins. In The Porphyrin Handbook (Kadish, K. M., Smith, K. M., and Guilard, R., Eds.) pp 185−298, Academic Press, San Diego.
34. Bertini, I., and Luchinat, C. (1996) NMR of Paramagnetic Substances. *Coord. Chem. Rev. 150*, 1–296.
35. Walker, F. A. (2000) Proton NMR and EPR Spectroscopy of Paramagnetic Metalloporphyrin. In The Porphyrin Handbook (Kadish, K. M., Smith, K. M., and Guilard, R., Eds.) pp 1−183, Academic Press, Boston.
36. La Mar, G. N. (2007) Application of the paramagnetic dipole field for solution NMR active site structure determination in low-spin, cyanide-inhibited ferric hemoproteins. *IUBMB Life 59*, 513–527.
37. Sandström, J. (1982) Dynamic NMR Spectroscopy, Academic Press, New York.
38. Richardson, J. S. (1981) The Anatomy and Taxonomy of Protein Structure. *Adv. Protein Chem. 34*, 167–339.